Predissociation spectra of the 35Cl–(H2) complex and its isotopologue 35Cl–(D2)

Miguel Lara-Moreno, Philippe Halvick, Thierry Stoecklin

PCCP

ROYAL SOCIETY OF CHEMISTRY

PAPER

View Article Online
View Journal

Cite this: DOI: 10.1039/d0cp05015f

Predissociation spectra of the $^{35}Cl^{-}(H_2)$ complex and its isotopologue $^{35}Cl^{-}(D_2)$†

Miguel Lara-Moreno, Philippe Halvick and Thierry Stoecklin *

Received 22nd September 2020,
Accepted 26th October 2020

DOI: 10.1039/d0cp05015f

rsc.li/pccp

The predissociation spectra of the $^{35}Cl^{-}(H_2)$ and $^{35}Cl^{-}(D_2)$ complexes are determined within an accurate quantum approach and compared to those recently measured in an ionic trap at 8 K and 22 K. The calculations are performed using an existing three-dimensional potential energy surface. A variational approach is used for the accurate quantum calculations of the rovibrational bound states. Several methods are compared for the search and the characterization of the resonant states. A good agreement between the calculated and measured spectra is obtained, despite a slight shift to the red of the calculated spectra. The comparison shows that only the *ortho* or *para* contribution is observed in the measured $^{35}Cl^{-}(H_2)$ or $^{35}Cl^{-}(D_2)$ spectrum, respectively. Quantum numbers are assigned to the rovibrational resonant states. It demonstrates that the main features observed in the measured predissociation spectra correspond to a progression in the intermonomer vibrational stretching mode.

1 Introduction

Several combined theoretical and experimental studies have been dedicated to the $^{35}Cl^{-}(H_2)$ and $^{35}Cl^{-}(D_2)$ complexes. The predissociation infrared spectra involving the $0 \rightarrow 1$ vibrational transition for H_2 or D_2 were first measured in 2001 by Wild *et al.*[1] Shortly after, Alexander[2] and Buchachenko *et al.*[3] computed the first *ab initio* potential energy surfaces (PES) and dipole moment surfaces for the $Cl^{-} + H_2$ collision. Buchachenko *et al.* also calculated the vibrational predissociation infrared spectra and obtained a very good agreement with the available experimental spectra measured by Wild *et al.* The photoelectron spectroscopy of $Cl^{-}(H_2)$ complex was also studied by Fergusson *et al.*[4] as a probe of the ClH_2 van der Waals potential well. The most recent work on this system was performed by Spieler *et al.*[5] who measured the low frequency combination bands in the region between 600 and 1100 cm^{-1} by infrared predissociation spectroscopy in a cryogenic 22-pole ion trap and using a free electron laser as a tunable light source at the FELIX Laboratory. A qualitative computation of the transition energies was also presented by Spieler *et al.*, however with only a partial agreement with the measured spectra, therefore motivating a more accurate theoretical work.

The present predissociation spectra are calculated using the PES of Buchachenko *et al.*[3] and following the lines of some of our previous works dedicated to the N_2H^{-},[6] SNH^{-}[7] or $He–C_3N^{-}$[8] molecular anions.

The paper is organized as follows. Section 2 is dedicated to the presentation of the method used to calculate the predissociation spectrum and to the presentation and comparison of the three different methods used for the determination of the resonant states. In Section 3, the theoretical results are compared with the experimental data while in Section 4 the main conclusions of our study are presented.

2 Theory

2.1 Spectroscopic intensities

If H_0 is the rovibrational Hamiltonian of the system while J and M are the quantum numbers associated respectively with the total angular momentum and its projection along the space-fixed z-axis, the wave function of any bound or quasi-bound rovibrational state i of the complex is solution of the equation:

$$H_0 \Psi_i^{JM} = E_{i,J} \Psi_i^{JM} \quad (1)$$

Using this notation the contribution to the infrared absorption coefficients for the transition $i,J \rightarrow i',J'$ of the spin isomer I, at temperature T and photon energy $\hbar\omega$, is proportional to the

Université de Bordeaux, ISM, CNRS UMR 5255, 33405, Talence, France.
E-mail: thierry.stoecklin@u-bordeaux.fr

† Electronic supplementary information (ESI) available: A table showing the convergence of the calculated energies *versus* the size of the basis set, a figure showing Argand diagrams of four low lying resonant states, four tables gathering the lowest rovibrational levels with their energy, parity and assigned quantum numbers for $J = 0$ and $J = 1$, two figures showing the convergence of the partition functions, two figures showing comparisons of the calculated and experimental spectra, and a figure showing the temperature dependence of the equilibrium constants for the ligand exchange reactions. See DOI: 10.1039/d0cp05015f

usual expression

$$\mathscr{I}^{I}_{i,J\to i',J'}(\omega,T) \propto \frac{g_I e^{-E_{i,J}/k_B T}}{Z(T)}\left(E_{i',J'} - E_{i,J}\right) S_{i,J\to i',J'} \times \rho_{i',J'}\left(E_{i,J} + \hbar\omega\right) \quad (2)$$

where g_I is the nuclear spin statistical weight,

$$Z(T) = \sum_{I,i,j} g_I (2J+1) e^{-E_{i,J}/k_B T} \quad (3)$$

is the rovibrational partition function of the complex and $S_{i,J\to i',J'}$ is the line strength defined as

$$S_{i,J\to i',J'} = \sum_{MM'} \left\| \left\langle \Psi^{J'M'}_{i'} | \vec{\mu} | \Psi^{JM}_{i} \right\rangle \right\|^2 \quad (4)$$

In order to take into account the width of the final state when it is a quasi bound state we included in eqn (2) the density of state $\rho_{i',J'}(E)$ in the vicinity of any final quasi-bound state. We furthermore use for $\rho_{i',J'}(E)$ the usual Breit–Wigner distribution[9] describing an isolated narrow resonance:

$$\rho_{i',J'}(E) = \frac{1}{\pi} \frac{\Gamma_{i',J'}/2}{\left(\mathscr{E}_{i',J'} - E\right)^2 + \left(\Gamma_{i',J'}/2\right)^2} \quad (5)$$

where $\mathscr{E}_{i',J'} = \mathrm{Re}\left(E_{i',J'}\right)$ and $\Gamma_{i',J'} = -2\,\mathrm{Im}\left(E_{i',J'}\right)$ are respectively the energy and the width of the resonance. The zero of energy was set to the energy of the ground state of the infinitely separated monomers.

2.2 Rovibrational energy levels and wave functions

The geometry of the $Cl^-(X_2)$ system (X = H or D) can be defined by the space-fixed Jacobi coordinates $\vec{r}$ and $\vec{R}$, where $\vec{r}$ is the X_2 internuclear vector, while $\vec{R}$ is the vector between the X_2 center of mass and the atom Cl^-. In these coordinates, the rovibrational Hamiltonian of the $Cl^-(X_2)$ system is

$$H_0 = -\frac{\hbar^2}{2\mu}\left[\frac{1}{R}\frac{\partial^2}{\partial R^2}R + \frac{l^2}{R^2}\right] + H_{X_2} + V(R,r,\theta) \quad (6)$$

where μ is the reduced mass of the system, H_{X_2} is the space-fixed Hamiltonian of the X_2 diatom, $\hat{l}$ is the relative orbital angular momentum operator and θ is the angle between $\vec{R}$ and $\vec{r}$. We use for $V(R,r,\theta)$ the interaction potential developed by Buchachenko *et al.*[3] This PES is based on coupled cluster calculations with single and double excitations and perturbative triple excitation, with the aug-cc-pVQZ basis set and midbond functions, and it is corrected from the basis set superposition error. The equilibrium structure of $Cl^-(H_2)$ is linear. The PES has therefore two potential wells equivalent by symmetry, related by the rotation of the H_2 molecule by an angle of π. The two wells are separated by a large energy barrier. Since the predissociation spectrum involves transitions between bound states and resonant states, we detail in the two following subsections the different methods used to compute the bound and resonant states.

2.2.1 Bound states. We use the same variational approach described in some of our previous works[6–8] which is here briefly reminded. The internal stretching motion of the complex is described by the vibrational energies ε_{vj} and wave-functions $\chi_{vj}(r)$ of the diatom where the indexes j and v respectively stand for its rotational and vibrational quantum numbers. They are obtained by solving the diatomic Schrödinger equation

$$\left[H_{X_2} - \varepsilon_{vj}\right]\chi_{vj}(r) Y_{jm_j}(\hat{r}) = 0 \quad (7)$$

using Chebyshev polynomials for the radial coordinate r.

The angular basis set for the whole system is expressed in the usual coupled angular momentum representation,

$$\mathscr{Y}^{JM}_{jl}(\hat{R},\hat{r}) = \sum_{m_j m_l} \left\langle jm_j lm_l | JM \right\rangle Y_{lm_l}(\hat{R})\, Y_{jm_j}(\hat{r}) \quad (8)$$

These functions are eigenfunctions of j^2, l^2, J^2, J_z and of the parity $\mathscr{P}$ operator with the eigenvalues $p = (-1)^{j+l}$. The rovibrational wave functions of the complex are then expanded in these basis sets as:

$$\Psi^{JM}_{i}(\vec{r},\vec{R}) = \frac{1}{rR}\sum_{vjl} G^{JMi}_{vjl}(R)\chi_{vj}(r)\mathscr{Y}^{JM}_{jl}(\hat{r},\hat{R}) \quad (9)$$

where Chebyshev polynomials are again used to expand the radial wave functions describing the stretching motion along the R coordinate. Further simplification in the calculations are obtained from the symmetry properties of the $\mathscr{Y}^{JM}_{jl}(\hat{R},\hat{r})$ wave functions under the operations of the G_4 permutation inversion group as shown in Table 1.

Since both $G^{JMi}_{vjl}(R)$ and $\chi_{vj}(r)$ are totally symmetric under the operations of the G_4 group, the symmetry of the rovibrational basis set (eqn (9)) can be classified using the irreps of the G_4 group. The full Hamiltonian equation is then solved separately for each irrep of the G_4 group. The convergence of the bound-state energies is checked as a function of the size of the basis set. As can be seen in Table S1 (see ESI†) the combination of 3 vibrational and 6 rotational states of the diatom together with a 200 point DVR grid along R spanning the $[3,30]a_0$ interval ensures a convergence of 0.001 cm^{-1}.

2.2.2 Resonances. Because of their non-$\mathscr{L}^2$ nature, the energies and wave functions of resonances are not straightforwardly obtained by approaches limited to a finite domain of space. We will here compare the performances of three different methods based on the representation of the Hamiltonian matrix in a finite-size box.

2.2.2.1 Stabilization method. Within this approach the unperturbed Hamiltonian H_0 is repeatedly diagonalized in basis sets of ever larger scattering coordinate R extension[10,11] while the angular and radial basis set associated with the r coordinate remain unchanged. In practice, we increase the size of the box, denoted by the parameter L, but keep the same number of DVR points,

Table 1 Classification of the symmetry-adapted angular basis set according to the values of j, l and p

j	l	p	Γ_{rovib}
e	e	+	A_1
e	o	−	A_2
o	e	−	B_1
o	o	+	B_2

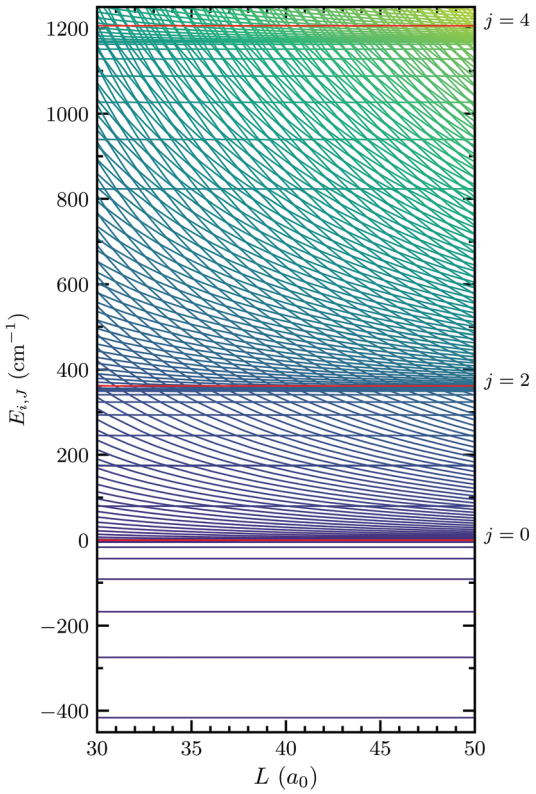

Fig. 1 Eigenvalues of H_0 for $J = 0$ and symmetry A_1 as a function of the size of the box spanned by the basis set. The red lines correspond to the asymptotic energy levels $Cl^- + p\text{-}H_2$ ($v = 0, j$).

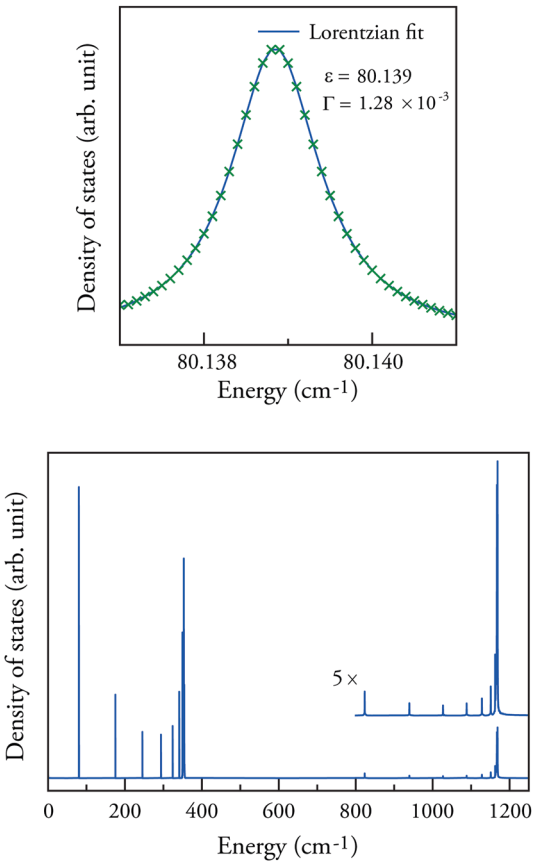

Fig. 2 Density of states for $J = 0$ and symmetry A_1. A zoom into the first resonance is shown in the upper panel.

provided that the number of points is large enough to compute accurate wave functions even for the largest box size.

Three kind of solutions are obtained which are associated with bound, resonant and continuum states. The latter are separated by an energy gap inversely proportional to the size of the box. The wave function of a resonance can be partitioned into an inner and an outer part. The inner part is the wave function of a quasi-bound state supported by the effective potential, then localized at short range, while the outer part is a wave function belonging to the continuum. The ratio of outer to inner amplitudes is usually proportional to the width of the resonance. The energy of the resonance is essentially determined by the inner part of the wave function, which can be stabilized within a finite-size box approach. Indeed, in the stabilization diagram (Fig. 1), the energies of the continuum states appear as decreasing functions of L, while the energies of resonances remain constant. Furthermore, the crossings between the continuum and the resonance energies are avoided crossings since both kind of states are coupled by the Hamiltonian. The energy gap of a given avoided crossing is directly related to the magnitude of the Hamiltonian matrix element between the two crossing states. Thus, a largely avoided crossing means a resonance with a large width and inversely, a narrowly avoided crossing means a small width.

This method give a good estimate of the resonance position $\mathscr{E}$ while only a qualitative information about the width Γ can be drawn from the energy shift of the avoided crossings. When $\Gamma \to 0$, the energy gap of the avoided crossings is also very small and thus the resonance position can be accurately obtained from the stable energy plateau. A few schemes[10–12] have been proposed to extract the resonance parameters from the stabilization diagram through the calculation of the density of states $\rho(E)$. Mandelshtam *et al.*[11] have shown that the density of states can be computed as:

$$\langle \rho_L^J(E) \rangle = \frac{1}{\Delta L} \sum_i \left| \frac{\mathrm{d}E_{i,J}(L)}{\mathrm{d}L} \right|^{-1}_{E_{i,J}(L')=E} \qquad (10)$$

where the derivatives of the energies $E_{i,J}$ *vs.* L are evaluated at the intersections of the $E_{i,J}(L)$ curves with the constant E line, *i.e.* $E_{i,J}(L') = E$, with L' in the range $L - \Delta L/2 < L' < L + \Delta L/2$. Each resonance is then fitted to the Lorentzian form of eqn (5) (see Fig. 2). The resulting positions and widths of the first low lying resonances are given in Table 2.

However, since the outer part of the resonance is not correctly calculated in a finite-size box, a small error on the resonance parameters can be expected. Another drawback of this method is its lack of information about the resonance wave function. These difficulties can be overcome by the complex absorbing potential (CAP) method.

Table 2 Comparison of the different approaches for determining the position $\mathscr{E}$ and width Γ of resonances belonging to the A_1 irrep and for J = 0. These parameters are given in cm^{-1}

Stabilization		CAP		$\langle 1/R^2 \rangle$
$\mathscr{E}$	Γ	$\mathscr{E}$	Γ	$\mathscr{E}$
80.139	0.0013	80.139	0.0013	80.143
175.049	0.0048	175.049	0.0046	175.051
245.289	0.0082	245.290	0.0082	245.295
293.608	0.0086	293.609	0.0088	293.600

2.2.2.2 Complex absorbing potential method. It has been shown recently[13] that this method gives results in good agreement with the direct extraction of the resonance parameters from close-coupling scattering calculations. Within this approach a non-Hermitian complex symmetric Hamiltonian matrix is built by adding an imaginary potential to H_0:

$$H(\eta) = H_0 - i\eta W(R) \quad (11)$$

where η is the strength of the CAP and $W(R)$ is a real positive function of the scattering R coordinate, which take here the simple form

$$W(R) = (R - R_0)^2\theta(R - R_0) \quad (12)$$

where R_0 is the starting point of the CAP and $\theta(x)$ is the Heaviside function. The addition of the CAP transforms the finite-size box into an infinite one since almost all reflections of the wave function on the outer bound of the box are suppressed. The resonance energies and wave functions are then obtained from the diagonalization of $H(\eta)$ in any $\mathscr{L}^2$-basis set. We here use the eigenfunctions of H_0 defined by eqn (9). Hence the matrix elements of $H(\eta)$ are

$$\left\langle \Psi_{i'}^{J'M'} | H(\eta) | \Psi_i^{JM} \right\rangle = E_{i,J}\delta_{ii'}\delta_{JJ'}\delta_{MM'} - i\eta \sum_{jklv} G_{vjl}^{JMi}(R_k) G_{vjl}^{JMi'}(R_k) W(R_k) \delta_{JJ'}\delta_{MM'} \quad (13)$$

where R_k denotes the Chebyshev DVR grid points. In order to reduce the computational effort, we removed the bound state eigenfunctions from the basis set $\{\Psi_i^{JM}\}$. We assume they are not coupled by the CAP with the continuum and resonant states if R_0 is larger than the external turning points. Also, we reduced the set of discretized continuum eigenfunctions to those lying below a given threshold E_{cut} chosen to ensure that the energy gap between the computed resonances and any state above the threshold is big enough to make sure that they are uncoupled.

Since we use a finite basis set, the resonance energies are found to vary as function of the strength η of the complex potential $W(R)$. The complex eigenvalues $E_{i,J}(\eta)$ of $H(\eta)$ computed for different values of η produce trajectories in the complex plane (see Fig. S1 in ESI†). A resonance is associated with a stability point which in the complex plane appears as a loop, a cusp or a sharp turn. This stability point provides the best approximation to the resonance position and width. The latter quantities for a few selected resonances are shown in Table 2 and a very good agreement with the results of the stabilization method is observed. The widths calculated here are larger by one or two orders of magnitude than those of the vibrational predissociation resonances[3] obtained by the vibrational excitation of H_2. This suggest that the inter-monomer modes of motion are more coupled with the continuum than the intra-monomer mode of motion.

However, both methods require to perform a large number of diagonalizations in order to achieve a good accuracy, thus requiring lengthy computational time. In the case of the CAP method, one can substantially reduces the size of the matrix to be diagonalized and save computer time, but the calculations have to be performed for each resonance. A cheaper alternative is fortunately available for the determination of the resonance energies as shown in the next section.

2.2.2.3 Rotational constant method. The widths of the computed resonances shown in Table 2 are much smaller than the energy gaps between resonance positions. Thus we can neglect them and, instead of the Breit–Wigner distribution for $\rho(E)$ defined in eqn (5), approximate $\rho(E)$ by a delta function centered at $\hbar\omega = \mathscr{E}_{i',J'} - E_{i,J}$. Since the stabilization calculations showed that the variation of the eigenvalues $E_{i,J}(L)$ of H_0 near a resonance is small when $\Gamma_{i,J} \to 0$, we can also take $\mathscr{E}_{i,J} = E_{i,J}$. We then assume that the energies of the resonant states are well approximated by the energies obtained by solving the eqn (1) in a finite domain of space. Finally, we use the fact that conversely to continuum states, narrow resonances are localized at short range. We can then clearly distinguish the resonant states from the continuum states in the discretized spectrum of H_0 by computing the average value of R^{-2}. The computed values represented in Fig. 3 are seen to be large for resonances while remaining small for the states of the continuum. The accuracy of the resonance energies calculated with this method (see Table 2) is seen to be better than 0.01 cm^{-1}. As a summary, two different approaches, the stabilization method and the CAP method, are in excellent agreement. This provide reference values for the positions of resonances on which the positions calculated with the more approximate rotational constant method can be compared. The good agreement observed in Table 2 validates the latter method which is easier to implement and was then used for computing the spectra.

2.2.3 Labeling of the states. In order to tentatively assign vibrational quantum numbers to each computed energy level, we made contour plots in the (R, θ) Jacobi coordinates of the associated wave functions and counted the number of nodes in each direction. We also additionally performed an harmonic normal mode analysis. The $Cl^-(X_2)$ (X = H, D) complexes have two equivalent linear equilibrium structures, related by the exchange of identical atoms. Four normal modes of vibration can be associated to each of these structures: the ΔR stretching mode, the doubly degenerate $\Delta\theta$ bending mode, and the Δr stretching mode, labeled respectively by the v_1, v_2, and v_3 quantum numbers. Besides these three quantum numbers, the vibrational wave function is defined by a fourth quantum

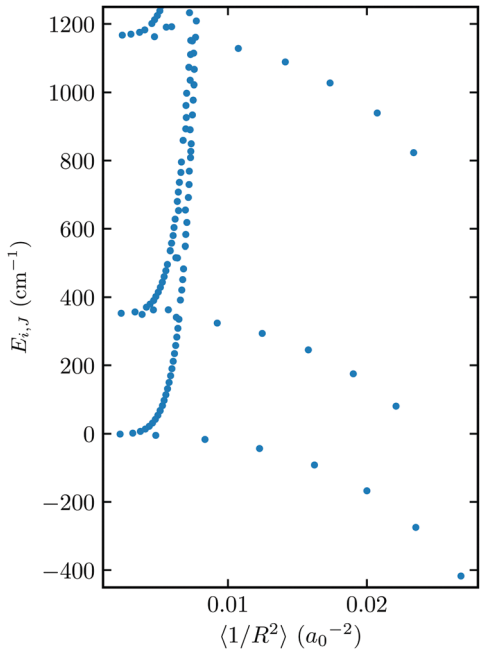

Fig. 3 Expected values of $\langle 1/R^2 \rangle$ for the H_0 eigenstates with the symmetry A_1 and $J = 0$, for the $Cl^-(H_2)$ complex.

number associated with the doubly degenerate bending mode. It is denoted here by l_2 and defines the projection of the vibrational angular momentum along the principal axis of the linear equilibrium structure. Lets us note that since the projection of the electronic orbital momentum along the latter axis is $\Lambda = 0$, then l_2 is equal to the projection of the total angular momentum J. Consequently for $J = 0$, only $l_2 = 0$ and even values of v_2 are possible.

The symmetry group of the rovibrational states of a linear heteronuclear molecule is the $C_{\infty v}(M)$ group[14] which is of order two. The two irreducible representations are labeled + and − depending on the eigenvalue p of the parity operator $\mathscr{P}$. This group applies to rigid molecules, *i.e.* to the molecular vibrations of a single equilibrium structure, while the G_4 group also contains the exchange of identical nuclei. A given level is labeled + if for $l_2 \geq 0$, $J + l_2$ is even or if for $l_2 < 0$, $J + l_2$ is odd. Conversely a level is labeled − if for $l_2 \geq 0$, $J + l_2$ is odd or if for $l_2 < 0$, $J + l_2$ is even. The symmetry of the vibrational wave functions is denoted Σ, Π, Δ,... for l_2 equal to 0, ±1, ±2,....

The correspondence between the irreducible representations of the $C_{\infty v}(M)$ and G_4 groups is shown in Table 1. We can see in this table that to each energy level calculated in the harmonic approximation and belonging to an irrep of the $C_{\infty v}(M)$ group, is corresponding a pair of degenerate levels belonging to the irreps of the G_4 group. The degeneracy of these levels is lifted when the complete double minimum PES is taken into account, owing to tunneling through the barrier separating the two equivalent linear equilibrium structures.

2.3 Dipole moment and line strength

We take the dipole moment to lie along the intermolecular vector $\vec{R}$ and to be proportional to R. This approximation has proved to be quite accurate in our previous studied dedicated to other atomic ion-diatom complexes like $H^-(N_2)$,[6] $H^-(CO)$[15] or $Na^+(H_2)$.[16] In the present case, this approximation is furthermore supported by the results obtained by Buchachenko *et al.*[3] The interested reader can find in any of these previous studies the expression of the dipole moment matrix elements from which result the selection rules: $\Delta p = 0$, $\Delta J = 0, \pm 1$, $\Delta j = 0$, $\Delta l = \pm 1$.

2.4 Nuclear spin statistics: *ortho* and *para* states

The total wave function $\Psi_{rovib} \times \Psi_{spin} \times \Psi_{elec}$ must be antisymmetric with respect to the interchange of the H atoms and symmetric with respect to the interchange of the D atoms. Therefore in the case of the $Cl^-(H_2)$ complex the total wave function symmetry is either B_1 or B_2 while in the case of $Cl^-(D_2)$ it is either A_1 or A_2. The electronic wave function Ψ_{elec} of both complexes belongs to the totally symmetric representation A_1. The rovibrational wave function can belong to any of the G_4 irreducible representations and its symmetry is determined by the one of the rotational basis set functions (see Table 1), which is independent of the nature of the complex.

There are $(2I_{Cl} + 1)(2I_H + 1)^2 = 16$ spin wave functions for the $^{35}Cl^-(H_2)$ complex, 12 are of symmetry A_1 corresponding to states with total spin $I = 5/2, 3/2, 1/2$ while the four remaining are of B_2 symmetry corresponding to states with total spin $I = 3/2$. This can be written $\Gamma_{spin} = 12A_1 \oplus 4B_2$.

In the case of the $^{35}Cl^-(D_2)$ complex, there are $(2I_{Cl} + 1)(2I_D + 1)^2 = 36$ spin wave functions. 24 are of A_1 symmetry corresponding to states with $I = 7/2, 5/2, 3/2, 1/2$ while the remaining are of B_2 symmetry corresponding to states with $I = 5/2, 3/2, 1/2$ This can written as: $\Gamma_{spin} = 24A_1 \oplus 12B_1$.

The statistical weights needed in eqn (2) are then straightforwardly obtained and are gathered in Table 3. Let us note that for both complexes, the *ortho* and *para* notation always refers respectively to the A_1 and B_2 irreps of the spin wave function. Since transitions between *ortho* and *para* states are forbidden one can consider them as two different species of the complex.

3 Results

The dissociation energies of $^{35}Cl^-(p\text{-}H_2)$, $^{35}Cl^-(o\text{-}H_2)$, $^{35}Cl^-(p\text{-}D_2)$ and $^{35}Cl^-(o\text{-}D_2)$ are found to be 416.5 cm^{-1}, 526.3 cm^{-1}, 581.1 cm^{-1}, and 521.7 cm^{-1}, respectively. Since the *para*/*ortho* parity is conserved by the dissociation process, the ground states of $^{35}Cl^-(o\text{-}H_2)$ and $^{35}Cl^-(p\text{-}D_2)$ correlate with the $j = 1$ rotational state of the diatomic product, of which the energy is included in the dissociation energy. The energy gap between the rovibrational ground state of the *ortho* and *para* species is

Table 3 Statistical weight (SW) of the rovibrational states

	$Cl^-(H_2)$			$Cl^-(D_2)$		
	Γ_{rovib}	Γ_{spin}	SW	Γ_{rovib}	Γ_{spin}	SW
para	A_1	B_2	4	B_1	B_2	12
	A_2	B_2	4	B_2	B_2	12
ortho	B_1	A_1	12	A_1	A_1	24
	B_2	A_1	12	A_2	A_1	24

8.89 cm^{-1} and 0.39 cm^{-1} for $^{35}Cl^{-}(H_2)$ and $^{35}Cl^{-}(D_2)$, respectively, showing that the mass effect on tunneling is significant here. For the levels with larger vibrational energy, the tunneling becomes easier as one get closer to the top of the isomerization barrier, and consequently the energy splitting increases, up to more than 100 cm^{-1}. Tables gathering the calculated energy, the assigned quantum numbers and the symmetry of the lowest lying levels are provided in the ESI† for both complexes and for $J = 0$ and $J = 1$.

The theoretical spectra presented in Fig. 4 and 5 have been obtained by assuming that the initial populations of the rovibrational levels of $^{35}Cl^{-}(H_2)$ or $^{35}Cl^{-}(D_2)$ are in thermal equilibrium at 8 or 22 K. Furthermore we assume that the experimental cooling down to 8 or 22 K is fast enough such that the *ortho* to *para* population ratios remain equal to the natural ratios at room temperature, namely 3 : 1 for H_2 and 2 : 1 for D_2. The rovibrational partition functions which are necessary for evaluating the Boltzmann distributions have been calculated with a maximal value of the total angular momentum $J_{max} = 20$. This value ensure the convergence of the partition functions (see Fig. S2 and S3 in ESI†) for both temperatures and thus an accurate calculation of the spectrum.

Fig. 4 shows a comparison between the calculated and experimental predissociation spectra of the $Cl^{-}(H_2)$ complex at 8 K. The energy differences between the calculated *ortho* and *para* bands results from the tunneling splitting which is quite large in the case of H atoms. As expected at this low temperature, all the transitions are departing from the ground state and we consequently labeled the bands by giving only the final states. Most of the bands are of Σ-type ($l_2 = 0$) and are associated with an increase of the number of quanta in the stretching mode ν_1. The main contribution to the experimental spectrum is due to the *ortho* complex. We can also see on Fig. 4 that the theoretical spectrum is shifted to the red by about 8 cm^{-1}. This discrepancy between theory and experiment which was already noticed by Buchachenko *et al.*[3] might be attributed to a lack of accuracy of the PES.

In the case of the $Cl^{-}(D_2)$ spectrum, the comparison between theory and experiment at a temperature of 22 K is shown in Fig. 5 Again most of the bands are of Σ-type although compared to $Cl^{-}(H_2)$ there is an increase in the number of Π-type bands which might be simply due to the higher temperature. Again the progression in the bands are associated with an increase of the number of quanta in the stretching mode ν_1 and the theoretical bands are also shifted to the red by about 8 cm^{-1}. As expected the separation between the *ortho* and *para* bands is much smaller than for $Cl^{-}(H_2)$ due to the heavier mass of the D atoms which have a lower probability of tunneling.

In order to finalize the comparison between theory and experiment, the theoretical spectra were shifted by 8 cm^{-1} and convolved using a linewidth broadening of 1 cm^{-1}. The comparison between theory and experiment is now easier to observe in Fig. 6 and 7. The contributions of both the *para* and *ortho* species are shown, as well as the resulting Boltzmann averaged spectrum. The agreement between theory and experiment is quite good and the main contributions to the spectra appear clearly to be provided by the $Cl^{-}(o\text{-}H_2)$ and $Cl^{-}(p\text{-}D_2)$ species. A second comparison of the $Cl^{-}(H_2)$ and $Cl^{-}(D_2)$ predissociation spectra was also made for the temperatures of 22 K and 8 K, respectively, showing a qualitative good agreement between theory and experiments (see Fig. S4 and S5 in ESI†).

The lack of experimental transitions belonging to the $Cl^{-}(p\text{-}H_2)$ and $Cl^{-}(o\text{-}D_2)$ complexes could be explained on the basis of the rapid ligand exchange reactions

$$Cl^{-}(p\text{-}H_2) + o\text{-}H_2 \rightarrow Cl^{-}(o\text{-}H_2) + p\text{-}H_2 \quad (14)$$

$$Cl^{-}(o\text{-}D_2) + p\text{-}D_2 \rightarrow Cl^{-}(p\text{-}D_2) + o\text{-}H_2 \quad (15)$$

as it was first proposed by Wild *et al.*[1] and subsequently investigated in more detail by Buchachenko *et al.*[3] and by Grinev *et al.*[17]

Using the dissociation energies calculated in this work, the reactions (14) and (15) are found to be exoergic by 109.8 cm^{-1}

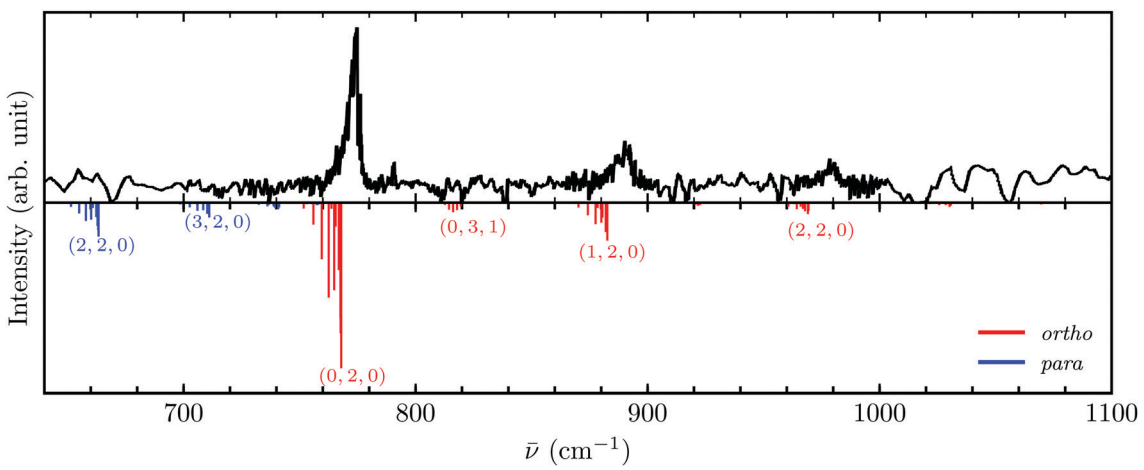

Fig. 4 Experimental (top) and theoretical (bottom) predissociation spectra of $Cl^{-}(H_2)$ at 8 K. Since all transition occur from the vibrational ground state, the bands have been labeled using the final state vibrational quantum numbers (v_1,v_2,l_2). Both spectra are normalized to unity at the maximum.

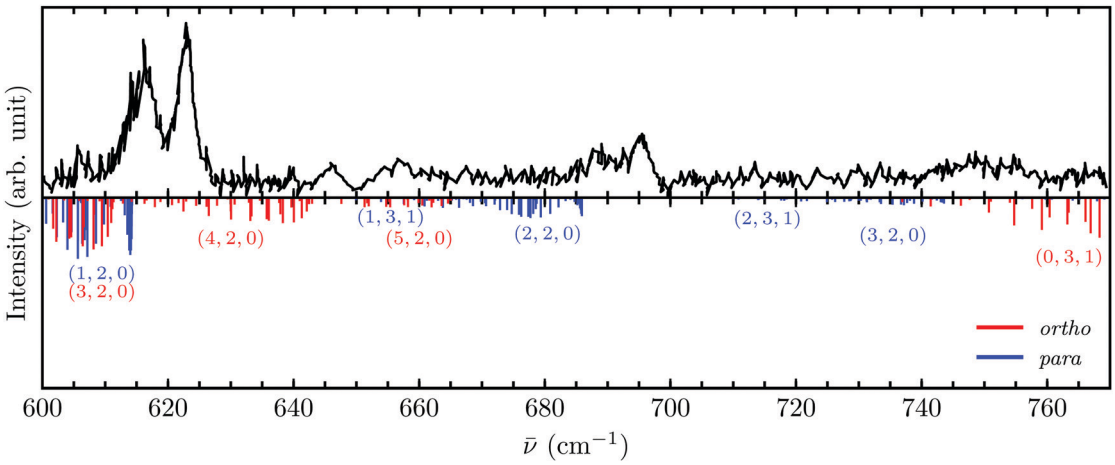

Fig. 5 Experimental (top) and theoretical (bottom) predissociation spectra of $Cl^-(D_2)$ at 22 K. Since all transition occur from the vibrational ground state, the bands have been labeled using the final state vibrational quantum numbers (v_1,v_2,l_2). Both spectra are normalized to unity at the maximum.

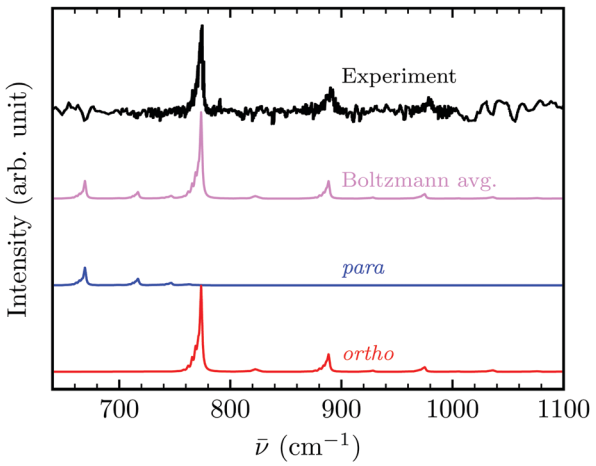

Fig. 6 Comparison between the experimental and convolved theoretical predissociation spectrum of $Cl^-(H_2)$ at 8 K assuming a linewidth broadening of about 1 cm^{-1}. The calculated spectra are shifted to the blue by 8 cm^{-1} to match the first experimental band. All spectra are normalized to unity at the maximum.

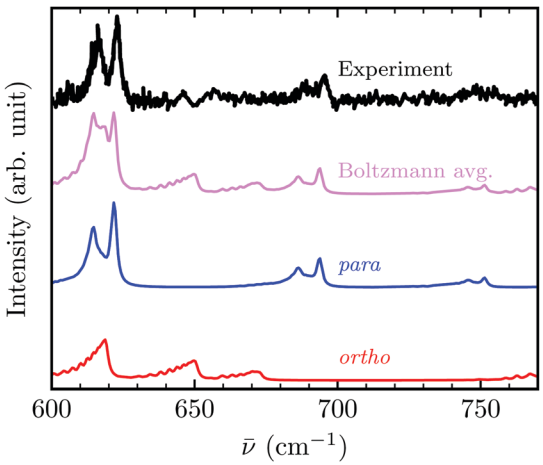

Fig. 7 Comparison between the experimental and convolved theoretical predissociation spectrum of $Cl^-(D_2)$ at 22 K assuming a linewidth broadening of about 1 cm^{-1}. The calculated spectra are shifted to the blue by 8 cm^{-1} to match the first experimental band. All spectra are normalized to unity at the maximum.

and 60.2 cm^{-1}, respectively. At a given temperature T, the products/reactants abundance ratio is given by the equilibrium constant $K(T)$ which can be easily calculated with the relative partition functions of the reactants and products,[17,18] Q_R and Q_P respectively,

$$K(T) = \exp\left(-\frac{\Delta E}{k_B T}\right)\frac{Q_P(T)}{Q_R(T)} \quad (16)$$

where ΔE is the energy of the products minus the energy of the reactants. The partition functions for the *ortho* and *para* species of the complexes are nearly equal since only a few rotational levels contribute to the partition functions at $T \leq 22$ K and the rotational constants of the *ortho* and *para* species are very close. The partition functions for the *ortho* and *para* species of the diatomic molecules are in a 1 : 3 ratio since only the ground rovibrational levels contribute with the degeneracy factor $2j + 1$. Thus at low temperature, the temperature dependence of the ligand exchange equilibrium constants is almost only determined by the exponential $\exp\left(-\frac{\Delta E}{k_B T}\right)$. Table 4 (and Fig. S6 in the ESI†) gives the accurately calculated values of the equilibrium constants by using the rovibrational energy levels obtained in this work by solving the Schrodinger eqn (1).

If we assume that the *ortho* to *para* abundance ratio is 3 : 1 for H_2 and 2 : 1 for D_2, the large values of the equilibrium constant imply that the abundance of $^{35}Cl^-(p\text{-}H_2)$ and $^{35}Cl^-(o\text{-}D_2)$ are negligible with respect to the abundance of $^{35}Cl^-(o\text{-}H_2)$ and $^{35}Cl^-(p\text{-}D_2)$, respectively, except for the deuterated reaction at 22 K since the $^{35}Cl^-(p\text{-}D_2)$ to $^{35}Cl^-(o\text{-}D_2)$ abundance ratio is expected to be 8. In Fig. 7, the *para* contribution appears to be much closer to the experimental spectrum than the Boltzmann average. This suggest that the *para* species of $Cl^-(D_2)$ is significantly more

Table 4 Calculated equilibrium constants of the ligand exchange reactions

Temperature (K)	Reaction (14)	Reaction (15)
8	1.2×10^8	1.5×10^4
22	4.3×10^2	1.6×10^1

abundant than the *ortho* species, in agreement with the chemical equilibrium resulting from the D_2 ligand exchange reaction.

4 Conclusions

The predissociation spectra of the $^{35}Cl^-(H_2)$ and $^{35}Cl^-(D_2)$ complexes were calculated by an accurate quantum method. To this aim, an existing 3D PES was used. The bound states were computed using a variational approach in the space-fixed frame while several methods were compared for the computations of the resonant quasi-bound states. The quantum numbers associated with the lower transitions were attributed using symmetry arguments. The rovibrational transition spectra were calculated for both isotopologues and compared with the recently measured experimental spectra respectively at 8 K and 22 K. The very good agreement obtained between theory and experiment validates the quality of both the PES and the quantum method selected for performing the bound and resonant states calculations. This comparison also shows that the *ortho* component is dominating the measured $^{35}Cl^-(H_2)$ spectra, while it is the *para* component for $^{35}Cl^-(D_2)$. This result is attributed to the rapid *para* $\leftrightarrow$ *ortho* conversion of the complexes by collision with H_2 or D_2 molecules inside the trap at low temperature. The main experimental bands are eventually assigned to the $^{35}Cl^-(o\text{-}H_2)$ combination bands $2\nu_2$, $\nu_1 + 2\nu_2$, $2\nu_1 + 2\nu_2$, and to the $^{35}Cl^-(p\text{-}D_2)$ combination bands $\nu_1 + 2\nu_2$, $2\nu_1 + 2\nu_2$, $3\nu_1 + 2\nu_2$.

Conflicts of interest

There are no conflicts to declare.

Acknowledgements

We thank Prof. Roland Wester, Drs. Olivier Dulieu, Maurice Raoult and Robert Wild for many helpful discussions. This research has been supported by the Agence Nationale de la Recherche (ANR Project COLD HMINUS). Computer time for this study was provided by the Mésocentre de Calcul Intensif Aquitain which is the computing facilities of Université de Bordeaux et Université de Pau.

Notes and references

1 D. A. Wild, P. S. Weiser, E. J. Bieske and A. Zehnacker, *J. Chem. Phys.*, 2001, **115**, 824–832.
2 M. H. Alexander, *J. Chem. Phys.*, 2003, **118**, 9637–9642.
3 A. A. Buchachenko, T. A. Grinev, J. Kłos, E. J. Bieske, M. M. Szcześniak and G. Chałasiński, *J. Chem. Phys.*, 2003, **119**, 12931–12945.
4 M. J. Ferguson, G. Meloni, H. Gomez and D. M. Neumark, *J. Chem. Phys.*, 2002, **117**, 8181–8184.
5 S. Spieler, D. F. Dinu, P. Jusko, B. Bastian, M. Simpson, M. Podewitz, K. R. Liedl, S. Schlemmer, S. Brünken and R. Wester, *J. Chem. Phys.*, 2018, **149**, 174310.
6 F. Lique, P. Halvick, T. Stoecklin and M. Hochlaf, *J. Chem. Phys.*, 2012, **136**, 244302.
7 Y. Ajili, T. Trabelsi, O. Denis-Alpizar, T. Stoecklin, A. G. Császár, M. Mogren Al-Mogren, J. S. Francisco and M. Hochlaf, *Phys. Rev. A*, 2016, **93**, 052514.
8 M. Lara-Moreno, T. Stoecklin and P. Halvick, *J. Chem. Phys.*, 2017, **146**, 224310.
9 N. Moiseyev, *Non-Hermitian Quantum Mechanics*, Cambridge University Press, 2011.
10 C. H. Maier, L. S. Cederbaum and W. Domcke, *J. Phys. B: At. Mol. Phys.*, 1980, **13**, L119–L124.
11 V. A. Mandelshtam, T. R. Ravuri and H. S. Taylor, *Phys. Rev. Lett.*, 1993, **70**, 1932–1935.
12 V. Ryaboy, N. Moiseyev, V. A. Mandelshtam and H. S. Taylor, *J. Chem. Phys.*, 1994, **101**, 5677–5682.
13 D. Papp, J. Sarka, T. Szidarovszky, A. G. Császár, E. Mátyus, M. Hochlaf and T. Stoecklin, *Phys. Chem. Chem. Phys.*, 2017, **19**, 8152–8160.
14 P. Bunker and P. Jensen, *Molecular Symmetry and Spectroscopy*, NRC Press, Canada, 1998.
15 T. Stoecklin, P. Halvick, M. Lara-Moreno, T. Trabelsi and M. Hochlaf, *Faraday Discuss.*, 2018, **212**, 101–116.
16 D. Burdakova, G. Nyman and T. Stoecklin, *Mon. Not. R. Astron. Soc.*, 2019, **485**, 5874–5879.
17 T. A. Grinev, A. A. Buchachenko and R. V. Krems, *ChemPhysChem*, 2007, **8**, 815–818.
18 P. Atkins and J. de Paula, *Atkins' Physical Chemistry*, W. H. Freeman and Company, 8th edn, 2006.

